$LiTaO_3:Bi^{3+},Tb^{3+},Ga^{3+},Ge^{4+}$

A Smart Perovskite with High Charge Carrier Storage Capacity for X-Ray Imaging, Stress Sensing, and Non-Real-Time Recording

Lyu, Tianshuai; Dorenbos, Pieter; Xiong, Puxian; Wei, Zhanhua

DOI
10.1002/adfm.202206024

Publication date
2022

Document Version
Final published version

Published in
Advanced Functional Materials

ADVANCED FUNCTIONAL MATERIALS
www.afm-journal.de

$LiTaO_3:Bi^{3+},Tb^{3+},Ga^{3+},Ge^{4+}$: A Smart Perovskite with High Charge Carrier Storage Capacity for X-Ray Imaging, Stress Sensing, and Non-Real-Time Recording

Tianshuai Lyu, Pieter Dorenbos, Puxian Xiong,* and Zhanhua Wei**

Developing X-ray or UV-light charged storage and mechanoluminescence (ML) materials with high charge carrier storage capacity is challenging. Such materials have promising utilization in developing new applications, for example, in flexible X-ray imaging, stress sensing, or non-real-time recording. Herein, the study reports on such materials; Bi^{3+}, Tb^{3+}, Ga^{3+}, or Ge^{4+} doped $LiTaO_3$ perovskite storage and ML phosphors. Their photoluminescence, thermoluminescence (TL), and ML properties are studied. The charge carrier trapping and release processes in the Bi^{3+}, Tb^{3+}, Ga^{3+}, or Ge^{4+} doped $LiTaO_3$ are explained by using the constructed vacuum referred binding energy diagram of $LiTaO_3$ including the energy level locations of unintended defects, Tb^{3+}, Bi^{3+}, and Bi^{2+}. The ratio of the TL intensity after X-ray charging of the optimized $LiTaO_3$:0.005Bi^{3+},0.006Tb^{3+},0.05Ga^{3+}, or $LiTaO_3$:0.005Bi^{3+},0.006Tb^{3+},0.05Ge^{4+} to that of the state-of-the-art BaFBr(I):Eu^{2+} is ≈1.2 and 2.7, respectively. Force induced charge carrier storage phenomena is studied in the Tb^{3+}, Bi^{3+}, Ga^{3+}, or Ge^{4+} doped $LiTaO_3$. Proof-of-concept compression force distribution sensing and X-ray imaging is demonstrated by using optimized $LiTaO_3$:0.005Bi^{3+},0.006Tb^{3+},0.05Ga^{3+} dispersed in a hard epoxy resin disc and in a silicone gel film. Proof-of-concept color-tailorable ML for anti-counterfeiting is demonstrated by admixing commercial ZnS:Cu^{+},Mn^{2+} with optimized $LiTaO_3$:0.005Bi^{3+},0.006Tb^{3+},0.05Ge^{4+} in an epoxy resin disc.

1. Introduction

Mechanoluminescence (ML) is known as a photon emission phenomenon from a material during mechanical force application, like grinding, compression, friction, scratching, or fracturing.[1] Many inorganic and organic compounds, like polymer organic crystals, sugar, and alkali halide crystals, show ML when atomic or chemical bonds are suddenly fractured.[2] It means that the compound crystal structures are physically damaged and the ML cannot be observed repeatedly. This feature limits their utilization in stress sensing-based applications. ML may also appear in a compound with elastic deformation during compression force application.[3] The crystal structure is not damaged, and reproducible ML can be observed upon repeating compression force cycles. If the ML intensity linearly increases with increasing the compression force, then stress distribution sensing application is to be expected. Compounds with intense and reproducible ML were not developed prior to the 21st century. It was not until 1996 that intense and reproducible ML was reported in ZnS:Mn^{2+}[4] and $SrAl_2O_4$:Eu^{2+}[5] which have been utilized to demonstrate promising application in force distribution sensing. However, both ZnS:Mn^{2+} and $SrAl_2O_4$:Eu^{2+} are hygroscopic. Their ML intensities will greatly decrease after exposure to water. There is an ongoing research to develop more intense and stable ML materials. During the past two decades, different inorganic compounds, like $LiNbO_3$,[6] $Li_{1-x}Na_xNbO_3$,[7] AZnOS (A = Ca, Sr, Ba),[8] $(Ca_{1-x}Sr_x)_8Mg_3Al_2Si_7O_{28}$,[9] $LiGa_5O_8$,[10]

T. Lyu, Z. Wei
Xiamen Key Laboratory of Optoelectronic Materials and Advanced Manufacturing
Institute of Luminescent Materials and Information Displays
College of Materials Science and Engineering
Huaqiao University
Xiamen 361021, China
E-mail: lv_tianshuai@126.com, lv_tianshuai@hqu.edu.cn; weizhanhua@hqu.edu.cn

P. Dorenbos
Faculty of Applied Sciences
Department of Radiation Science and Technology
Delft University of Technology
Mekelweg 15, 2629JB Delft, The Netherlands

P. Xiong
School of Physics and Optoelectronics
Guangdong Provincial Key Laboratory of Fiber Laser Materials and Applied Techniques
Guangdong Engineering Technology Research and Development Center of Special Optical Fiber Materials and Devices
The State Key Laboratory of Luminescent Materials and Devices
South China University of Technology
Guangzhou 510640, China
E-mail: msxiong.puxian@mail.scut.edu.cn

The ORCID identification number(s) for the author(s) of this article can be found under https://doi.org/10.1002/adfm.202206024.

DOI: 10.1002/adfm.202206024

$KZn(PO_3)_3$,[11] $NaCa_2GeO_4F$,[12] MgF_2,[13] or $RE_2O_2S:Ln^{3+}$ (RE = Y, Lu, La, Gd)[14] were explored. Compared with traditional phosphors, the numbers of compounds that can show repeatable ML are still very limited. Unfortunately, the $ZnS:Mn^{2+}$ and $SrAl_2O_4:Eu^{2+}$ are still the state-of-the-art ML phosphors. One reason is that many compounds were studied by a trial-and-error approach only for force sensing-based applications.[15] Another reason is that the energy level locations of defects in different compounds are often not known, and then the mechanism behind charge carrier capturing and release processes associated with ML cannot be revealed. Since the ML mechanism remains unknown, rational exploration and optimization of ML materials is still challenging.

Although intense and repeatable ML compounds have promising utilization in developing new generation tactile sensors, rapid light emission from a ML compound when compression force is applied needs to be constantly measured by using an expensive photodetector, like photomultiplier tubes. This feature then limits the application to real-time compression force distribution sensing. In ref. [16], a new force-induced charge carrier storage phenomenon was observed in Eu^{2+}, Dy^{3+}, or Yb^{3+} doped $MSi_2O_2N_2$ (M = Ba, Sr) afterglow phosphors with traps. Promising applications in non-real-time recording of hand writing and vehicle collision traces were demonstrated by using a composite film with $BaSi_2O_2N_2:Eu^{2+},Dy^{3+}$ dispersed in silica gel. To the best of our knowledge, rare reports are published to discuss the force-induced charge carrier storage phenomenon.[17]

An afterglow or storage phosphor is a compound that can capture and temporarily store the free electrons and holes in defects-based traps during ionization radiation or high-energy photon excitation, like X-ray, gamma ray, or 254 nm UV-light.[18] The properties of the electron–hole recombination and luminescence centers determine the emission wavelength and decay time in a compound.[18a,19] The duration of the charge carriers in traps is determined by their trapping depths and the distribution in the compound lattices.[20] The energy level locations of charge carrier trapping centers are important to discuss and for rational design of new afterglow and storage phosphors.[21] In 2012, the chemical shift model was developed in ref. [22] to construct a so-called vacuum referred binding energy (VRBE) diagram. Such VRBE diagram enables one to compare the binding energies at the conduction band bottom, valence band top, or different defects in various compounds with a common reference energy.[23]

Similar to $LiNbO_3$, lithium tantalate ($LiTaO_3$) has a perovskite crystal structure. It crystallizes in a trigonal phase with an R3c space group at room temperature. $LiTaO_3$ perovskite combines special piezoelectric, pyroelectric, and optical properties,[24] resulting in promising utilization in piezoelectric sensors, nonlinear optics, and pyroelectric nuclear fusion. Since $LiTaO_3$ perovskite has a high density of ≈7.46 g cm^{-3}, it has a high X-ray absorption coefficient. $LiTaO_3$ is, therefore, a good compound to exploit X-ray charged afterglow and storage phosphors. Tb^{3+} or Pr^{3+} doped $LiTaO_3$ were studied in ref. [25], where the charge carrier capturing and release processes remained unclear. Bi^{3+} doped $LiTaO_3$ was studied in ref. [26], where it remained unclear whether Bi^{3+} acts as an electron or hole capturing and recombination center or not. In our previous work in ref. [17], the VRBE diagram of $LiTaO_3$ containing the energy level locations of Bi^{3+}, Bi^{2+}, and different lanthanides has been constructed that was used to address above unclear mechanisms. However, it has not been fully utilized to exploit ML, afterglow, or storage phosphor. To the best of our knowledge, the force-induced charge carrier storage phenomenon is not reported in the Tb^{3+} or/and Bi^{3+} doped $LiTaO_3$ perovskite yet.

Figure 1a shows the VRBE diagram of $LiTaO_3$ perovskite including the energy level locations of unintended defects, Tb^{3+}, Bi^{3+}, and Bi^{2+} as was established in ref. [17]. Generally, Bi^{3+} has a dual role. It could act both as an electron and as a hole capturing center in an inorganic compound.[18c] In Figure 1a, the $Bi^{2+2}P_{1/2}$ ground state is below the conduction band bottom. Bi^{3+} can capture an electron from the conduction band, forming Bi^{2+} in its ground state. Bi^{3+} then acts as an electron trap.[20a,27] The $Bi^{3+1}S_0$ ground state is above the valence band top. Bi^{3+} can capture a hole from the valence band, forming Bi^{4+} in a metastable state. Bi^{3+} then acts as a hole trapping center.[18b,28]

Figure 1a predicts that Bi^{3+} acts as an electron capturing center, while Tb^{3+} and Bi^{3+} act as the hole capturing and recombination centers. Based on this prediction, Tb^{3+} or/and Bi^{3+} doped $LiTaO_3$ storage phosphors were synthesized and analyzed (see Figures S4–S7, Supporting Information). Their TL glow curves after 254 nm UV-light or X-ray charging are shown in Figure 1b,c. However, their ML properties remain unknown. In this work, the ML properties of Tb^{3+} or/and Bi^{3+} doped $LiTaO_3$ will be studied. Ga^{3+} or Ge^{4+} was co-doped in $LiTaO_3:Bi^{3+},Tb^{3+}$ by a trial-and-error approach to improve the thermoluminescence (TL) and ML properties. Bi^{3+}, Tb^{3+}, Ga^{3+}, or Ge^{4+} doped $LiTaO_3$ perovskite storage, and ML phosphors with high charge carrier storage capacity were developed. The charge carrier trapping and release processes in the Bi^{3+}, Tb^{3+}, Ga^{3+}, or Ge^{4+} doped $LiTaO_3$ will be explained by using the constructed VRBE diagram including the energy level locations of unintended defects, Tb^{3+}, Bi^{3+}, and Bi^{2+}. The ratio of the integrated TL intensity after X-ray charging of the optimized $LiTaO_3$:0.005Bi^{3+},0.006Tb^{3+},0.05Ga^{3+} or $LiTaO_3$:0.005Bi^{3+},0.006Tb^{3+}, 0.05Ge^{4+} to that of the commercial $BaFBr(I):Eu^{2+}$ is ≈1.2 and 2.7, respectively. More than 40 h Tb^{3+} afterglow is measurable in the optimized $LiTaO_3$:0.005Bi^{3+},0.001Tb^{3+} and $LiTaO_3$:0.005Bi^{3+}, 0.006Tb^{3+},0.05Ge^{4+} after X-ray or 254 nm UV-light charging. Force induced charge carrier storage and ML phenomena will be studied in the Tb^{3+}, Bi^{3+}, Ga^{3+}, or Ge^{4+} doped $LiTaO_3$. We will demonstrate that the ML process is related to the release of the stored charge carriers when compression force is applied. Proof-of-concept compression force distribution sensing and X-ray imaging will be demonstrated by using optimized $LiTaO_3$:0.005Bi^{3+},0.006Tb^{3+},0.05Ga^{3+} dispersed in a hard epoxy resin disc and in a silicone gel film. Proof-of-concept color-tailorable ML for anti-counterfeiting will be demonstrated by admixing commercial $ZnS:Cu^{+},Mn^{2+}$ with optimized $LiTaO_3$:0.005Bi^{3+},0.006Tb^{3+},0.05Ge^{4+} in an epoxy resin disc.

2. Results

2.1. Charge Carrier Trapping and Release Processes in Bi^{3+}, Tb^{3+}, Ga^{3+}, or Ge^{4+} Doped $LiTaO_3$ Perovskite

Figure 2a shows the TL glow curves of Ga^{3+} or Ge^{4+} co-doped $LiTaO_3$:0.005Bi^{3+},0.006Tb^{3+} after X-ray charging. The

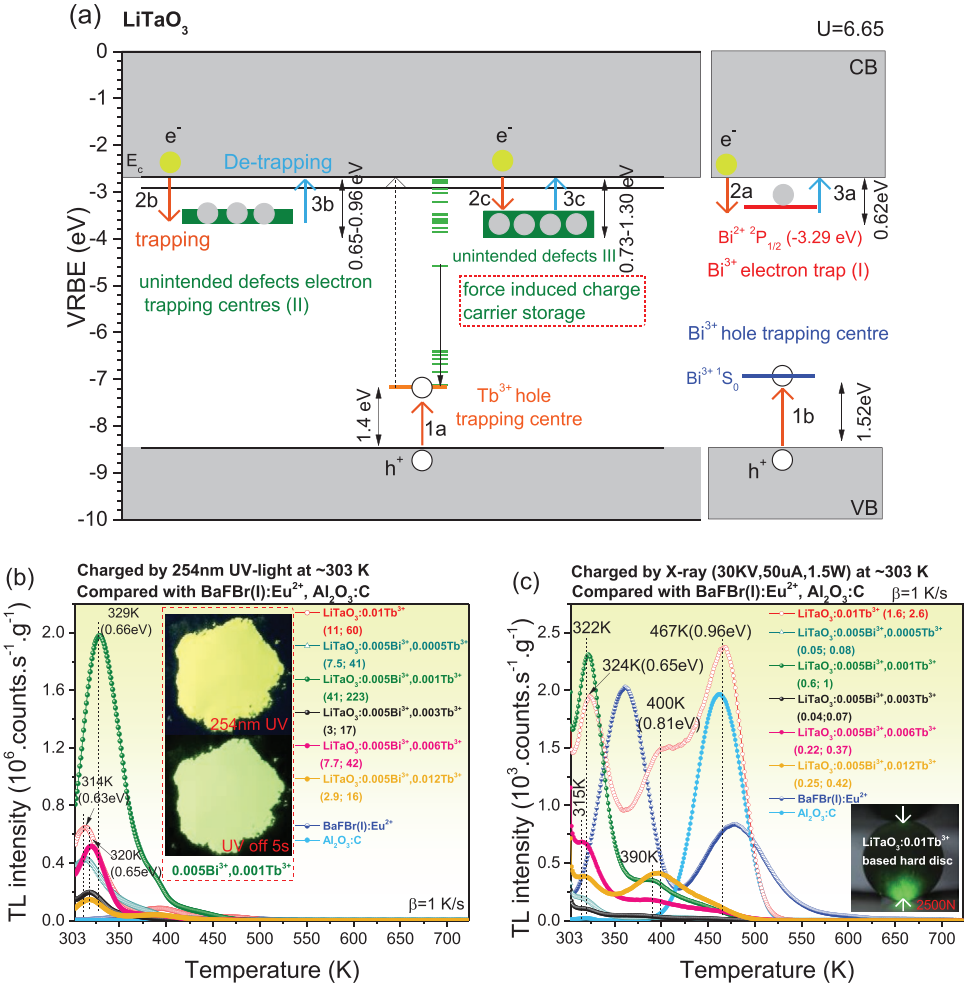

Figure 1. a) Vacuum referred binding energy (VRBE) diagram for $LiTaO_3$ containing the energy level locations of unintended defects, Tb^{3+}, Bi^{3+}, and Bi^{2+}. TL glow curves of $LiTaO_3$:0.005Bi^{3+},xTb^{3+} after b) 254 nm UV-light or c) X-ray charging. The trapping and release processes in (a) are denoted by solid arrows (1a until 3c), which will be explained in the text. The ratios denoted as (r1; r2) of integrated TL intensities from 303 to 723 K of $LiTaO_3$:0.005Bi^{3+},xTb^{3+} to that of (r1) the commercial BaFBr(I):Eu^{2+} or (r2) Al_2O_3:C chip are shown in the legend in (b) and (c). The inset in (b) shows the afterglow photograph of $LiTaO_3$:0.005Bi^{3+},0.001Tb^{3+} after 254 nm UV-light charging. The inset in (c) shows compression force distribution sensing by using the $LiTaO_3$:0.01Tb^{3+} dispersed in a hard epoxy resin disc.

$LiTaO_3$:0.005Bi^{3+},0.006Tb^{3+} in Figure 2a was newly synthesized and its TL intensity is about a factor of two lower than that in Figure 1c. The ratios (r1; r2) of the integrated TL intensities between 303 and 700 K of the Ga^{3+} or Ge^{4+} co-doped $LiTaO_3$:0.005Bi^{3+},0.006Tb^{3+} to that of the state-of-the-art BaFBr(I):Eu^{2+} (r1) and Al_2O_3:C chip (r2) are provided in the legend of Figure 2a. Compared with non co-doped $LiTaO_3$:0.005Bi^{3+},0.006Tb^{3+}, the integrated TL intensity increases ≈9 or 13 times after co-doping of Ge^{4+} or Ga^{3+}. The $LiTaO_3$:0.005Bi^{3+},0.006Tb^{3+},0.05Ga^{3+} and $LiTaO_3$:0.005Bi^{3+}, 0.006Tb^{3+},0.05Ge^{4+} share common TL glow peaks near ≈322, ≈382, ≈416, and ≈443 K, which are related to unintended electron trapping centres. Their trapping depths can be estimated and shown in the legend of Figure 2a by utilizing Equation S1 (Supporting Information) with the T_m values, $\beta = 1$ K s^{-1}, and the frequency factor of 1.07×10^9 s^{-1}.

Figure 2b shows the TL glow curves of Ga^{3+} or Ge^{4+} co-doped $LiTaO_3$:0.005Bi^{3+},0.006Tb^{3+} after 254 nm UV-light charging. The ratios (r1) of the integrated TL intensities between 303 and 700 K of the Ga^{3+} or Ge^{4+} co-doped $LiTaO_3$:0.005Bi^{3+},0.006Tb^{3+} to that of $LiTaO_3$:0.005Bi^{3+},0.006Tb^{3+} are shown in the legend of Figure 2b. Compared with $LiTaO_3$:0.005Bi^{3+},0.006Tb^{3+}, the integrated TL intensity increases ≈3 times with the co-doping of Ga^{3+} or Ge^{4+}. Intense Tb^{3+} 4f→4f afterglow appears in $LiTaO_3$:0.005Bi^{3+},0.006Tb^{3+},0.05Ga^{3+} and $LiTaO_3$:0.005Bi^{3+}, 0.006Tb^{3+},0.05Ge^{4+} in the dark after 254 nm UV-light charging (see Figure S9, Supporting Information).

To further optimize the charge carrier storage capacity in $LiTaO_3$:0.005Bi^{3+},0.006Tb^{3+},0.05Ge^{4+}, it was synthesized at a higher temperature of 1275 °C with a duration of 6 h. Figure 2c shows the TL glow curve of the optimized $LiTaO_3$:0.005Bi^{3+},0.006Tb^{3+}, 0.05Ge^{4+} after 200 s X-ray charging. TL glow peaks at ≈328, ≈398, and ≈446 K appear at $\beta = 1$ K s^{-1}. The ratios (r1; r2; r3) of the integrated TL intensity from 303 to 700 K of $LiTaO_3$:0.005Bi^{3+}, 0.006Tb^{3+},0.05Ge^{4+} to that of the state-of-the-art (r1) BaFBr(I):Eu^{2+}, (r2) Al_2O_3:C chip, and the (r3) optimized $NaLuF_4$:Tb^{3+} from

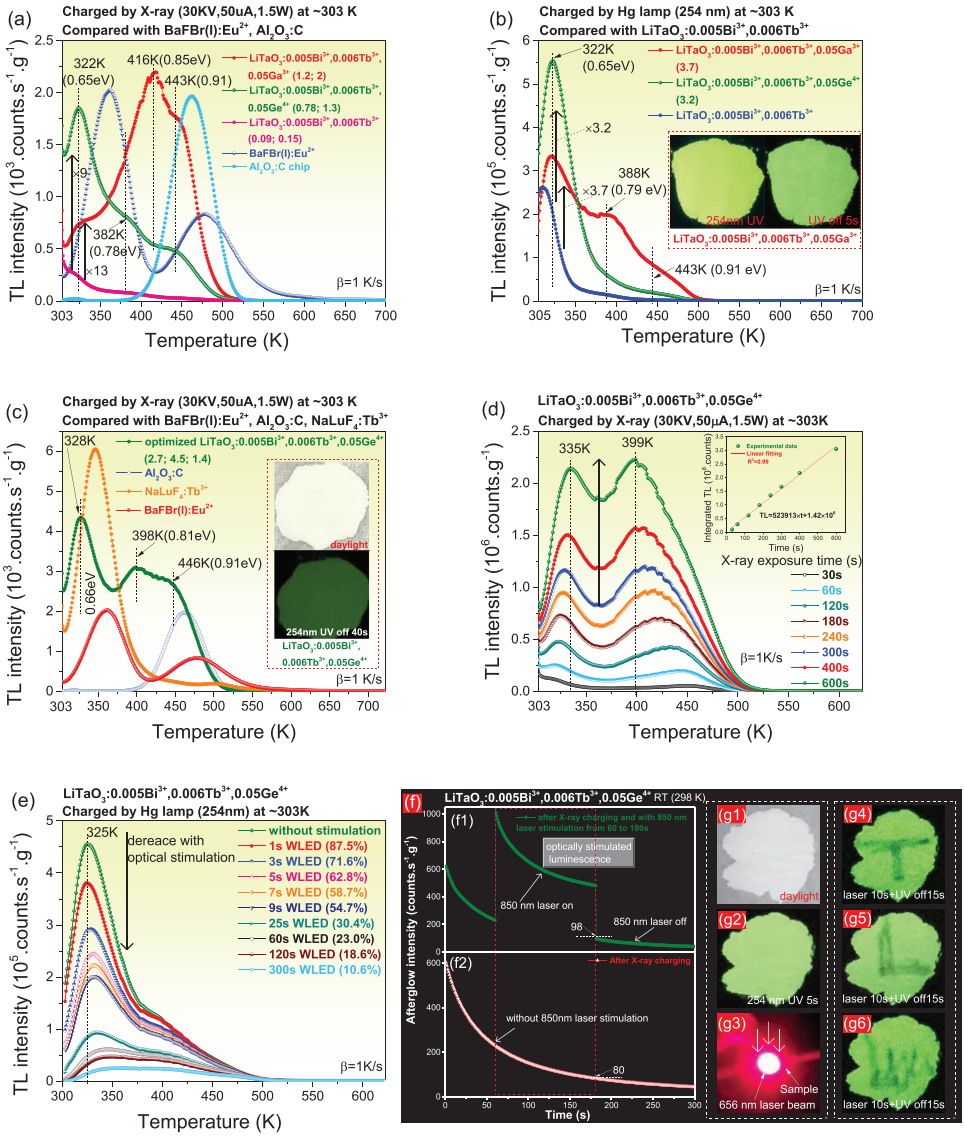

Figure 2. TL glow curves at $\beta = 1$ K/s of Ga^{3+} or Ge^{4+} co-doped $LiTaO_3$:0.005Bi^{3+},0.006Tb^{3+} after a) X-ray or b) 254 nm UV-light charging. TL glow curves of the optimized $LiTaO_3$:0.005Bi^{3+},0.006Tb^{3+},0.05Ge^{4+} after c) 200 s X-ray charging, d) after exposure to X-ray with a duration from 30 until 600 s, and e) after 254 nm UV-light charging and then followed by WLED stimulation with different duration time. f) RT isothermal decay curves after X-ray charging and then followed by 120s 850 nm stimulation, and (g1) until (g6) information display of "T", "L", and "Lyu" by using the Tb^{3+} afterglow and the 656 nm laser stimulated emission behavior in the 254 nm UV-light charged $LiTaO_3$:0.005Bi^{3+},0.006Tb^{3+},0.05Ge^{4+}. The ratios of the integrated TL intensities of the Ga^{3+} or Ge^{4+} co-doped $LiTaO_3$:0.005Bi^{3+},0.006Tb^{3+} to that of the state-of-the-art BaFBr(I):Eu^{2+}, Al_2O_3:C chip, $NaLuF_4$:Tb^{3+}, or $LiTaO_3$:0.005Bi^{3+},0.006Tb^{3+}, respectively, are shown in the legends of panels (a) to (c).

the authors in ref. [30] are determined to be 2.7, 4.5, and 1.4, respectively.

Figure 2d shows the TL glow curves of the optimized $LiTaO_3$:0.005Bi^{3+},0.006Tb^{3+},0.05Ge^{4+} after X-ray charging with a duration from 30 until 600 s at ≈303 K. The integrated TL intensity from 303 to 600 K as a function of X-ray charging time is shown in the inset of Figure 2d, which can be fitted by a linear fitting formula of TL = 523 913 × t + 1.42 × 10^6. The same applies to $LiTaO_3$:0.005Bi^{3+},0.006Tb^{3+},0.05Ga^{3+} in Figure S14b (Supporting Information). It means that the optimized $LiTaO_3$:0.005Bi^{3+},0.006Tb^{3+},0.05Ge^{4+} and $LiTaO_3$:0.005Bi^{3+},0.006Tb^{3+},0.05Ga^{3+} can be used as potential dosimeters for X-ray detection.

Figure 2e shows the TL glow curves of $LiTaO_3$:0.005Bi^{3+},0.006Tb^{3+},0.05Ge^{4+} charged first by a Hg lamp (254 nm UV-light) and then followed by WLED stimulation with a duration from 1 until 300 s. The integrated TL intensities from 303 to 600 K by WLED stimulation to that of without stimulation are shown as a percentage value in the legend of Figure 2e. 1s or 300s WLED stimulation (52 mW cm^{-2}) liberates ≈13% or ≈90% of the stored electrons and holes, respectively. The same applies to $LiTaO_3$:0.005Bi^{3+},0.006Tb^{3+},0.05Ga^{3+} in Figure S16f (Supporting Information). The TL glow peak at ≈325 K decreases in $LiTaO_3$:0.005Bi^{3+},0.006Tb^{3+},0.05Ge^{4+} with both WLED and 656 nm laser stimulation (See Figure S16d, Supporting Information).

Weaker afterglow is to be expected in the phosphor area that was stimulated by a WLED lamp or 656 nm red laser stimulation. We utilized this phenomenon to demonstrate different afterglow texts of "T", "L", and "Lyu" in the dark in Figure 2g4 until Figure 2g6 by a 656 nm red laser beam as illustrated in Figure 2g3. The same applies to $LiTaO_3$:0.005Bi^{3+},0.006Tb^{3+} in Figure S17 (Supporting Information) and $LiTaO_3$:0.005Bi^{3+}, 0.006Tb^{3+},0.05Ga^{3+} in Figure S18 (Supporting Information).

Figure 2f1 shows the room temperature isothermal decay curve of $LiTaO_3$:0.005Bi^{3+},0.006Tb^{3+},0.05Ge^{4+} charged by X-ray and then followed by 850 nm infrared light stimulation from 60 until 180 s in the dark. Strong Tb^{3+} 4f→4f emissions emerge because the stored electrons and holes are quickly released during the 850 nm infrared laser stimulation. Note that ≈20% stronger afterglow appears at times after 180 s in the phosphor area that was stimulated by the 850 nm infrared laser as compared to Figure 2f2 recorded without stimulation. This is because the TL peak shifts slightly from ≈325 to 323 K with 850 nm stimulation, and there is a redistribution of charge carriers as demonstrated in Figure S16g (Supporting Information). Apparently in the redistribution, carriers from deep traps are transported to the trap responsible for afterglow thus enhancing afterglow with 20%.

Figure 3a shows the RT isothermal decay curves of Bi^{3+}, Tb^{3+}, Ga^{3+}, or Ge^{4+} doped $LiTaO_3$ after X-ray charging. The optimized $LiTaO_3$:0.005Bi^{3+},0.006Tb^{3+},0.05Ge^{4+}, and $LiTaO_3$:0.005Bi^{3+}, 0.001Tb^{3+} show strong initial afterglow intensity. More than 40 h Tb^{3+} 4f→4f emissions are measurable in $LiTaO_3$:0.005Bi^{3+}, 0.006Tb^{3+},0.05Ge^{4+} and $LiTaO_3$: 0.005Bi^{3+},0.001Tb^{3+} in the dark after 200 s X-ray charging in Figure 3b.

2.2. Force Induced Charge Carrier Trapping Processes

Figure 4a shows the TL glow curves of $LiTaO_3$:0.005Bi^{3+},0.006Tb^{3+}, 0.05Ga^{3+} charged by grinding in an agate mortar with different durations from 0 until 600 s in the dark. TL glow peaks at ≈381, ≈505, and ≈630 K appear. Their corresponding electron trapping depths are determined to be 0.77, 1.04, and 1.30 eV by using Equation 1 with T_m values, β = 1 K s^{-1}, and s = 1.07 × 10^9 s^{-1}, respectively. The integrated TL intensity between 303 and 723 K linearly increases with increasing grinding time from 0 to 600 s (see Figure S19a, Supporting Information).

Figure 4b shows the TL glow curves of $LiTaO_3$:0.005Bi^{3+}, 0.006Tb^{3+},0.05Ge^{4+} charged by grinding in an agate mortar with different durations from 0 until 300 s in the dark. TL glow peaks at ≈362, ≈441, ≈506, and ≈617 K emerge. Their corresponding electron trapping depths can be estimated to be 0.73, 0.90, 1.04, and 1.28 eV by utilizing Equation 1 with the experimentally observed T_m values, β = 1 K s^{-1}, and s = 1.07 × 10^9 s^{-1}, respectively. The integrated TL intensity from 303 to 723 K as a function of grinding time is shown in Figure 4c, which can be fitted by TL = 4410 × t + 47 948. It means that one can roughly estimate the amount of the force-induced charge carrier storage by using the equation with given time (*t*). The force-induced charge carrier storage phenomenon and a linear relation between the integrated TL intensity and the grinding time also appear in other Tb^{3+} or/and Bi^{3+} doped $LiTaO_3$ in Figures S20–S24 (Supporting Information).

Figure 4d compares the TL glow curves of $LiTaO_3$:0.005Bi^{3+}, 0.006Tb^{3+},0.05Ge^{4+} charged by X-ray, 254 nm UV-light, or grinding in an agate mortar. Two new TL glow peaks at ≈506 and 617 K appear by grinding. The similar applies to $LiTaO_3$:0.005Bi^{3+},0.006Tb^{3+},0.05Ga^{3+} in Figure S19b (Supporting Information) and other $LiTaO_3$:0.005Bi^{3+},xTb^{3+} in Figures S20c–S23c (Supporting Information).

2.3. ML and its Applications in Anti-Counterfeiting and Compression Force Distribution Sensing

The compression force-induced luminescence, also known as the ML phenomenon, was first explored in the Bi^{3+} and/or Tb^{3+} doped $LiTaO_3$ compounds. The ML spectra of $LiTaO_3$:0.005Bi^{3+}, xTb^{3+} (*x* = 0.0005–0.012), and $LiTaO_3$:0.01Tb^{3+} dispersed in hard epoxy resin discs when 1000 N compression force was applied in the dark are shown in Figure S25a1–6 (Supporting Information). Characteristic Tb^{3+} 4f→4f emissions appear upon compression force application. A 2D plot of the ML spectra in Figure S26a (Supporting Information) and the integrated ML intensity from 200 to 1000 nm as a function of Tb^{3+} concentration (x)

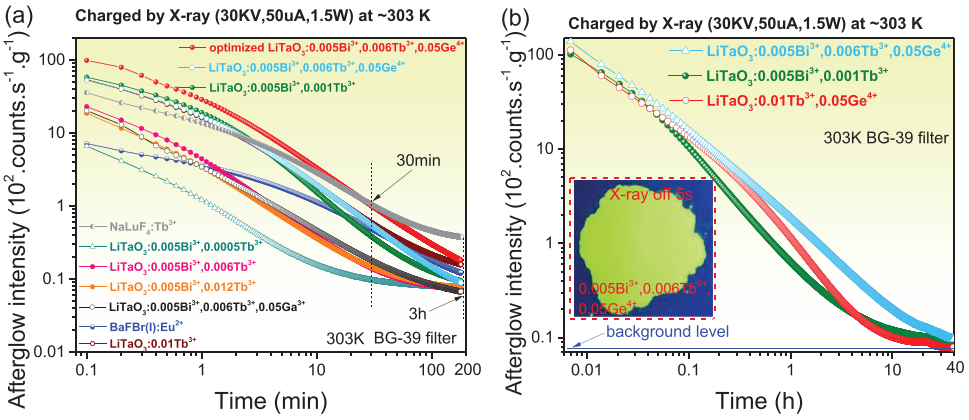

Figure 3. a) Three and b) 40 h room temperature isothermal decay curves of the Ga^{3+}, Ge^{4+}, Bi^{3+}, and/or Tb^{3+} doped $LiTaO_3$ after X-ray charging. The emission from 350 to 750 nm was monitored. The afterglow intensities were corrected by the sample mass and radiation time. The inset in (b) shows the afterglow photograph of $LiTaO_3$:0.005Bi^{3+},0.006Tb^{3+},0.05Ge^{4+} after X-ray charging in the dark.

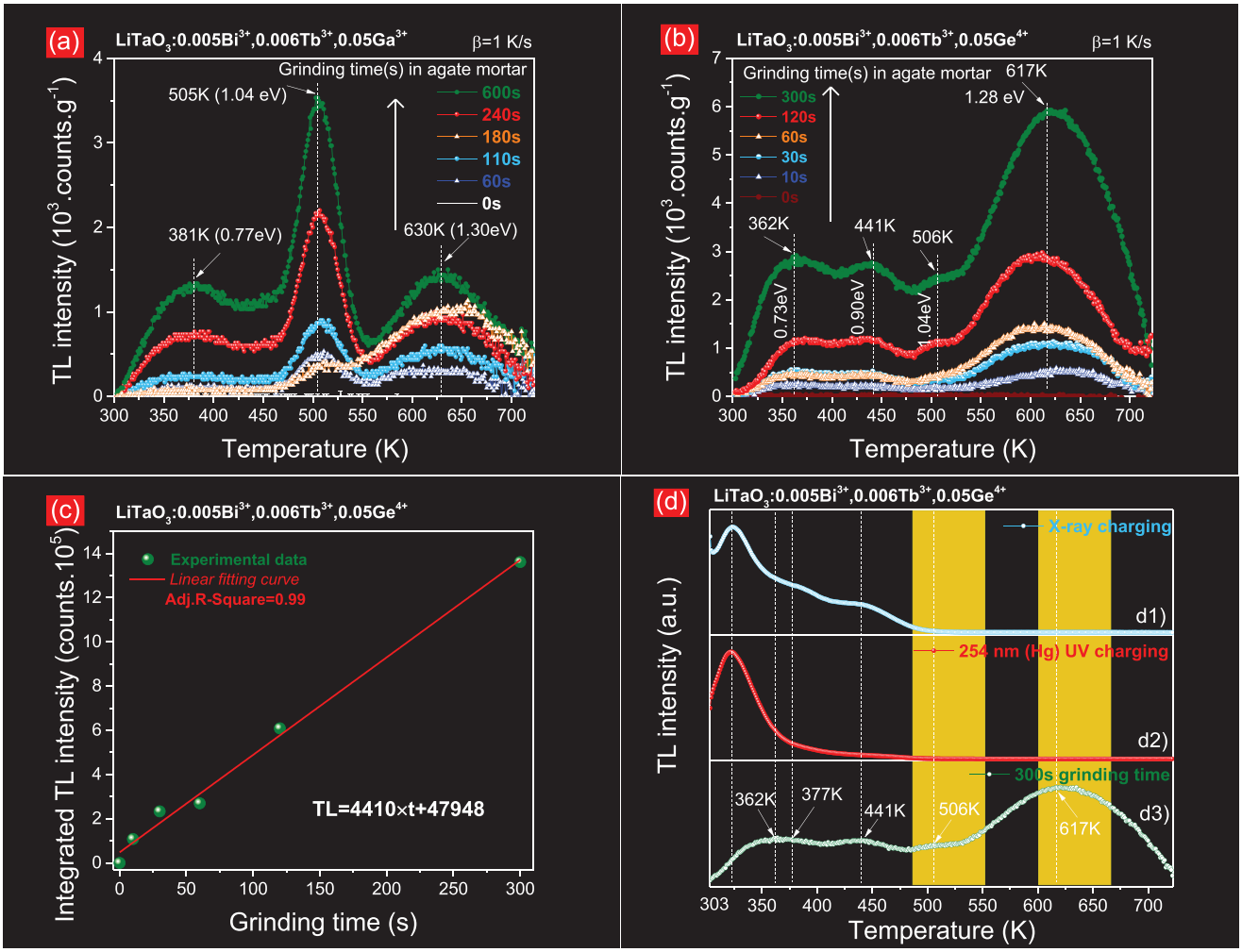

Figure 4. TL glow curves charged by different grinding time in an agate mortar for a) $LiTaO_3$:0.005Bi^{3+},0.006Tb^{3+},0.05Ga^{3+} and b) $LiTaO_3$:0.005Bi^{3+}, 0.006Tb^{3+},0.05Ge^{4+}. c) Integrated TL intensities between 303 to 723 K as a function of grinding time and d) a comparison of TL glow curves charged by X-ray, 254 nm UV-light, or 300s grinding time in an agate mortar. The Tb^{3+} 4f→4f emissions were monitored and a heating rate (β) of 1 K/s was used during TL measurements.

in Figure S26b (Supporting Information) demonstrate that the $LiTaO_3$:0.005Bi^{3+},0.001Tb^{3+} has the strongest ML intensity. This is consistent with the result in Figure 1b where $LiTaO_3$:0.005Bi^{3+},0.001Tb^{3+} has also the strongest integrated TL intensity after 254 nm UV-light charging. We therefore studied $LiTaO_3$:0.005Bi^{3+},0.001Tb^{3+} further.

Figure 5a shows the ML spectra of $LiTaO_3$:0.005Bi^{3+}, 0.001Tb^{3+} as a function of compression force in the dark. To decrease the effect of the afterglow on the ML process, the 254 nm UV-light charged $LiTaO_3$:0.005Bi^{3+},0.001Tb^{3+}-based epoxy resin disc was stored in the dark during 120 s prior to ML measurements. The integrated ML intensity from 200 to 1000 nm as a function of compression force (N) is shown in the inset of Figure 5a, which can be fitted by ML = 5.32 × N-170.44. The threshold of the compression force for ML is determined to be ≈32 N by this linear fitting formula. The above results indicate that the $LiTaO_3$:0.005Bi^{3+},0.001Tb^{3+} dispersed in a hard epoxy resin disc can be used as a potential sensor for force distribution sensing.

Figure 5b1–b4 demonstrates how to observe the compression force-induced luminescence (ML) by using the $LiTaO_3$:0.005Bi^{3+}, 0.001Tb^{3+}-based hard epoxy resin disc as an example in the dark. Figure 1b and its insets show that $LiTaO_3$:0.005Bi^{3+}, 0.001Tb^{3+} has strong afterglow at RT. Such afterglow will lead to difficulty in observing the ML phenomenon, as demonstrated in Figure 5b2. There are relatively shallow traps responsible for the RT afterglow in $LiTaO_3$:0.005Bi^{3+},0.001Tb^{3+}, and stored charge carriers in both shallow and deep traps are emptied when 1000 N compression force is applied. With increasing the waiting time from 20 to 120 s at RT in Figure 5b3, most stored charge carriers in shallow traps are emptied by afterglow, and charge carriers in deep traps are remaining. Those traps are emptied when 2500 N compression force is applied, leading to ML that appears in the areas indicated by the red dotted arcs.

To unravel the ML processes, Tb^{3+} single doped $LiTaO_3$ was studied. A $LiTaO_3$:0.01Tb^{3+}-based hard epoxy resin disc was first charged by a 15 W Hg lamp (254 nm UV-light) and then stored in the dark for 120 h prior to ML measurements. Figure 5c

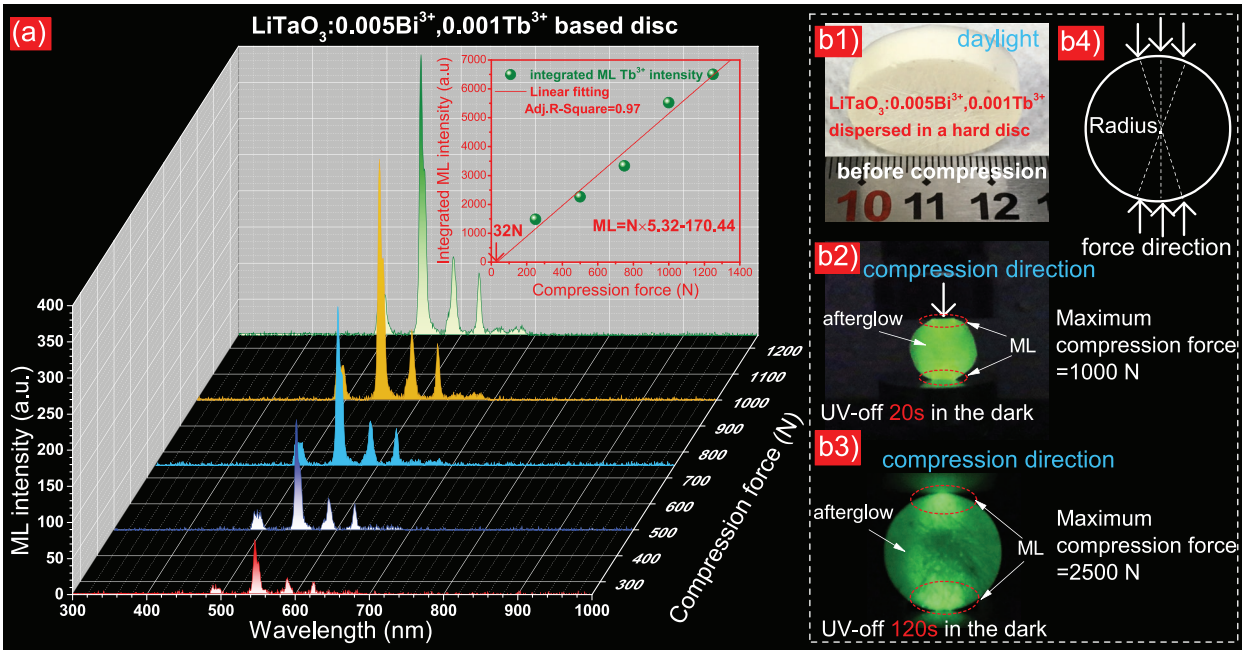

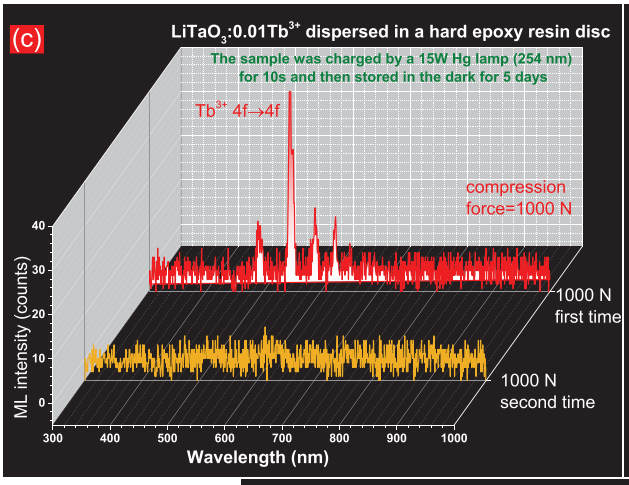

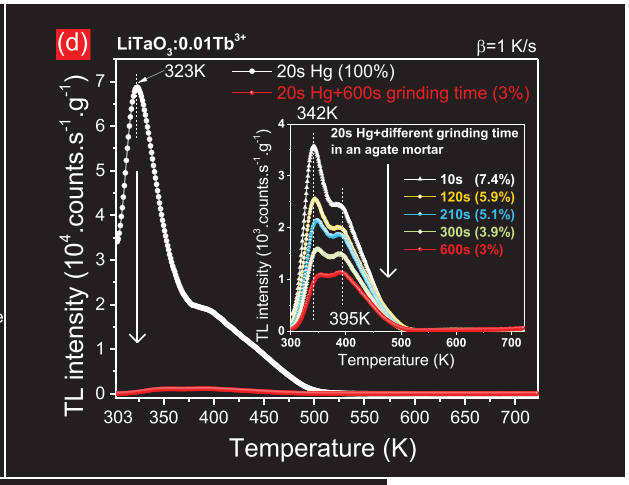

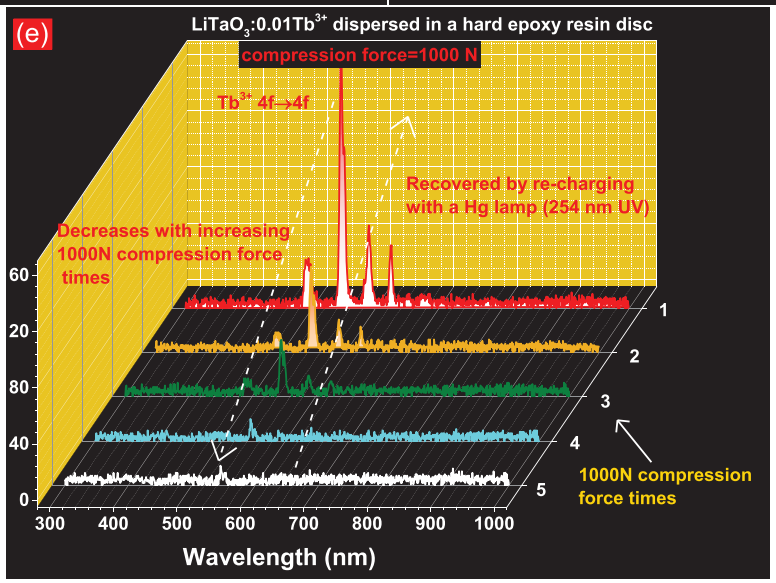

shows that the ML phenomenon appears only when the first time 1000 N compression force was applied. It means that ML liberates the stored charge carriers from deep traps. Since the traps are already empty no ML was observed anymore when the compression force was applied a second time. Figure 5d shows the TL glow curves of $LiTaO_3$:0.01Tb^{3+} charged first by 254 nm UV-light and then followed by grinding in an agate mortar with different durations from 0 until 600 s. The ratios of the integrated TL intensities between 303 and 700 K of $LiTaO_3$:0.01Tb^{3+} by grinding to that without grinding are shown in the legend of Figure 5d. The integrated TL intensity gradually decreases with increasing grinding time. The integrated TL remains only 3% after 600 s grinding.

A $LiTaO_3$:0.01Tb^{3+} based disc was first charged by a 15 W Hg lamp (254 nm UV-light) and then stored in the dark during 300 s prior to ML measurements. Compression force was applied to the disc from 0 to 1000 N for a few seconds in the dark and kept at 1000 N for ≈1 s for ML spectrum recording. We call this process as process 1. The disc was not re-charged by 254 nm UV-light and after ≈5 s, process 1 was repeated four times. Figure 5e shows the sequence of ML spectra where the integrated ML intensity decreases gradually to about zero with each following compression force. The ML intensity can be recovered to its maximum value by re-charging with a Hg lamp illumination. In Figure 5c, ML appears in $LiTaO_3$:0.01Tb^{3+}-based disc only when first time compression force is applied. This is because a large part of stored charge carriers in $LiTaO_3$:0.01Tb^{3+} was faded at RT during 120 h after 254 nm UV-light charging in the dark. The above results demonstrate that the ML phenomenon is controlled by the amount of the stored charge carriers in $LiTaO_3$:0.01Tb^{3+} during 254 nm UV-light charging.

To get more intense ML intensity for advanced applications, co-doping of Ga^{3+} or Ge^{4+} in $LiTaO_3$:0.005Bi^{3+},0.006Tb^{3+} was exploited. **Figure 6**a shows the ML spectra of the Ga^{3+} or Ge^{4+} co-doped $LiTaO_3$:0.005Bi^{3+},0.006Tb^{3+} and the $LiTaO_3$:0.005Bi^{3+}, 0.001Tb^{3+}-based discs when 1000 N compression force was applied in the dark. The integrated ML intensities from 300 to 1000 nm as a function of compound composition are shown in Figure 6b. $LiTaO_3$:0.005Bi^{3+},0.006Tb^{3+},0.05Ga^{3+} has the strongest integrated ML intensity. This is consistent with the TL result in Figure 2b where $LiTaO_3$:0.005Bi^{3+},0.006Tb^{3+}, 0.05Ga^{3+} has also the strongest integrated TL intensity after 254 nm UV-light charging. To obtain even stronger ML intensity, $LiTaO_3$:0.005Bi^{3+},0.006Tb^{3+},0.05Ge^{4+} was synthesized at 1275 °C with a duration of 6 h. Figure 6c shows that compared with the $LiTaO_3$:0.005Bi^{3+},0.006Tb^{3+},0.05Ga^{3+}-based epoxy resin disc, a 2.1 times stronger Tb^{3+} 4f→4f ML intensity appears when 1000 N compression force was applied. This is consistent with the TL result in Figure 2c where the optimized $LiTaO_3$:0.005Bi^{3+}, 0.006Tb^{3+}, 0.05Ge^{4+} has a high charge carrier storage capacity.

Figure 7a shows the ML spectra of $LiTaO_3$:0.005Bi^{3+}, 0.006Tb^{3+},0.05Ga^{3+} based disc as a function of compression force (*N*) in the dark. The integrated ML intensities between 300 and 1000 nm as a function of compression force are shown in the inset of Figure 7a, which can be fitted by ML = 0.83 × N-76.61. The minimum value of the observable compression force by the ML phenomenon is determined to be ≈92 N by this linear relation. The linearly increasing ML intensity has been utilized to detect the compression force distribution for the $LiTaO_3$:0.005Bi^{3+},0.006Tb^{3+},0.05Ga^{3+} based disc as demonstrated in Figure 7b.

Figure 7c shows the ML spectra of $LiTaO_3$:0.005Bi^{3+}, 0.006Tb^{3+},0.05Ga^{3+}-based disc charged first by 254 nm UV-light illumination and then followed by a sequence of 1000 N compression force applications. The integrated ML intensity gradually decreases. The maximum ML intensity can be recovered by re-charging with a Hg lamp (254 nm UV-light).

To explore color-tailorable ML for anti-counterfeiting application, a disc mechanical force sensor with a thickness of ≈0.6 cm and a diameter of ≈2.5 cm was fabricated by combining the epoxy resin, the optimized $LiTaO_3$:0.005Bi^{3+}, 0.006Tb^{3+},0.05Ge^{4+}, and commercial ZnS:Cu^{+},Mn^{2+}. The structure of the sensor is illustrated in Figure 7d where both the $LiTaO_3$:0.005Bi^{3+},0.006Tb^{3+},0.05Ge^{4+} and ZnS:Cu^{+},Mn^{2+} phosphors are uniformly dispersed inside the sensor. The ZnS:Cu^{+},Mn^{2+} is a good ML phosphor that can give intense orange emission when weak compression force is applied.[1a,31] The optimized $LiTaO_3$:0.005Bi^{3+},0.006Tb^{3+},0.05Ge^{4+} phosphor can give intense Tb^{3+} 4f→4f emissions when relatively large compression force is applied. Proof-of-concept color-tailorable recording of a hand writing trace for anti-counterfeiting application is demonstrated in Figure 7e,f. In Figure 7e, the text "bbQ" was written on the disc mechanical force sensor by using a metal pen with weak compression force, yielding orange ML dominantly from ZnS:Cu^{+},Mn^{2+}. In Figure 7f, the letter "b" was written on the disc mechanical force sensor by utilizing a glass pen with weak and strong compression forces, leading to orange ML from ZnS:Cu^{+},Mn^{2+} and green ML from $LiTaO_3$: 0.005Bi^{3+},0.006Tb^{3+},0.05Ge^{4+}.

2.4. Exploring X-Ray Imaging Application with the Optimized $LiTaO_3$:0.005Bi^{3+},0.006 Tb^{3+},0.05Ga^{3+} Storage Phosphor

A flexible film, called film X, with a diameter of ≈6 cm was synthesized by dispersing the optimized $LiTaO_3$:0.005Bi^{3+}, 0.006Tb^{3+}, 0.05Ga^{3+} storage phosphor in silicone gel as shown in **Figure 8**a(1). The film X was placed underneath three big wire connectors in Figure 8a(2). After exposure to X-rays, the wire connectors were removed. The X-ray charged film X was then heated to ≈330 K to obtain the X-ray imaging photograph in Figure 8a(3) by using the thermally stimulated Tb^{3+} 4f→4f emissions from $LiTaO_3$:0.005Bi^{3+},0.006Tb^{3+},0.05Ga^{3+} in the dark. To verify the resolution of the X-ray imaging, the

Figure 5. a) Mechanoluminescence (ML) spectra as a function of compression force and b1–b4) demonstration of the compression force induced luminescence from the 254 nm UV-light charged $LiTaO_3$:0.005Bi^{3+},0.001Tb^{3+} dispersed in a hard epoxy resin disc. c) ML spectra of $LiTaO_3$:0.01Tb^{3+} based disc charged first by 254 nm UV-light, faded in dark for 5 days, and then stimulated by applying 1000 N compression force, d) TL glow curves of $LiTaO_3$:0.01Tb^{3+} first charged by 254 nm UV-light and then followed by different grinding time in an agate mortar, e) repeatability test of ML spectra when 1000 N compression force was applied repeatedly for the $LiTaO_3$:0.01Tb^{3+} based disc after 254 nm UV-light charging. The inset in (a) shows the integrated ML intensities from 300 to 1000 nm as a function of compression force.

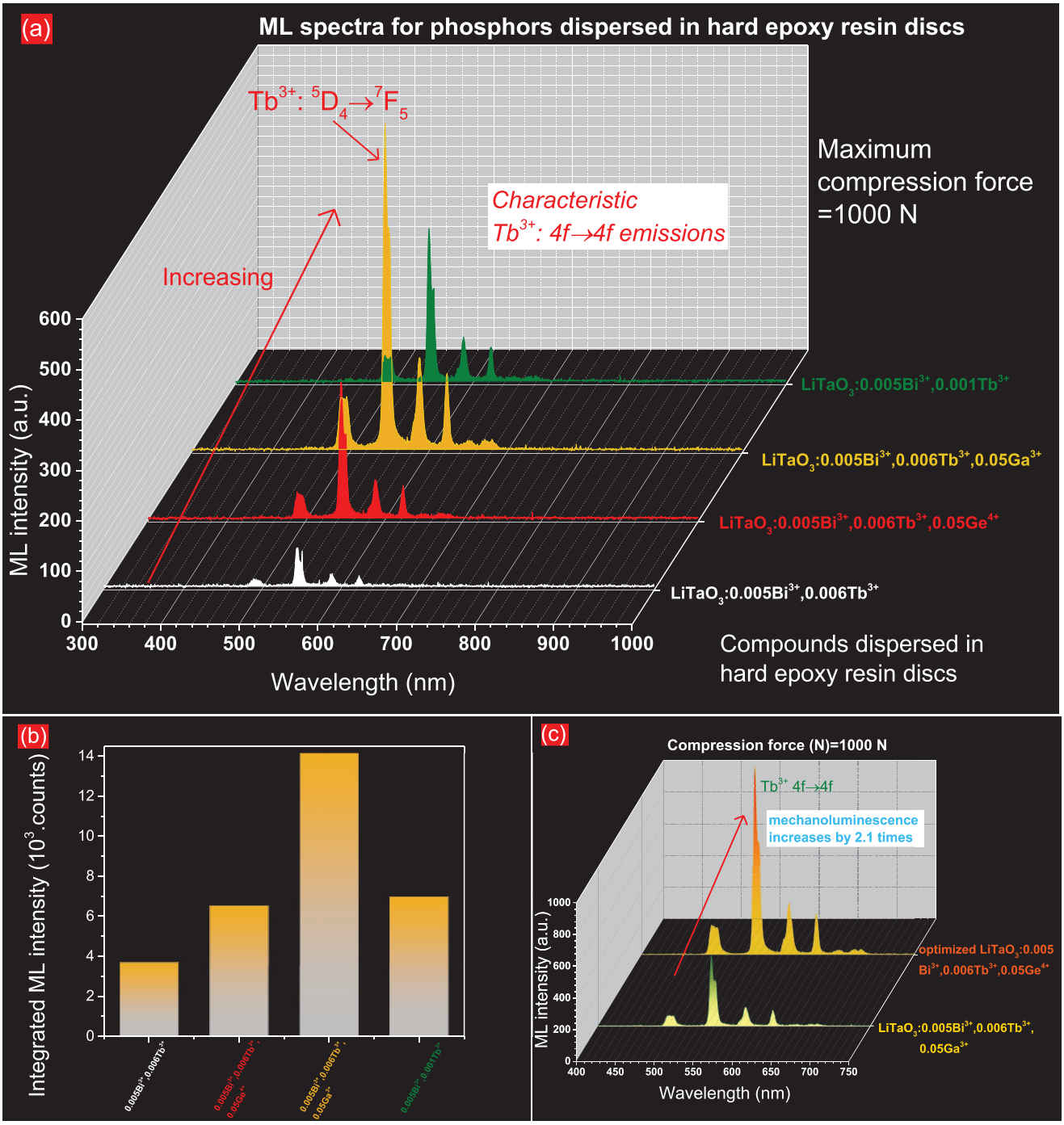

Figure 6. a) Mechanoluminescence (ML) and b) integrated ML intensities between 300 and 1000 nm for the Ga^{3+}, Ge^{4+}, Bi^{3+}, and/or Tb^{3+} doped $LiTaO_3$ dispersed in hard epoxy resin discs. c) A comparison of the ML spectra of the optimized $LiTaO_3$:0.005Bi^{3+},0.006Tb^{3+},0.05Ge^{4+} and $LiTaO_3$:0.005Bi^{3+},0.006 Tb^{3+}, 0.05Ga^{3+} based discs. The used comparison force was 1000 N.

film X was placed underneath a Pb-based resolution test plate as demonstrated in Figure 8b(1), which was then exposed to X-rays. The test plate was first removed after X-ray charging and the film X was then heated to ≈330 K in the dark to get the X-ray imaging photograph in Figure 8b(2). A resolution of about 5 line pairs mm^{-1} (lp mm^{-1}) was obtained as shown in Figure 8b(3).

3. Discussion

3.1. Charge Carrier Trapping and Release Processes

The vacuum referred binding energy (VRBE) diagram of $LiTaO_3$ containing the ground state energy level locations of Bi^{2+}, Bi^{3+}, and Tb^{3+} in Figure 1a shows that Tb^{3+} and Bi^{3+} act as ≈1.4

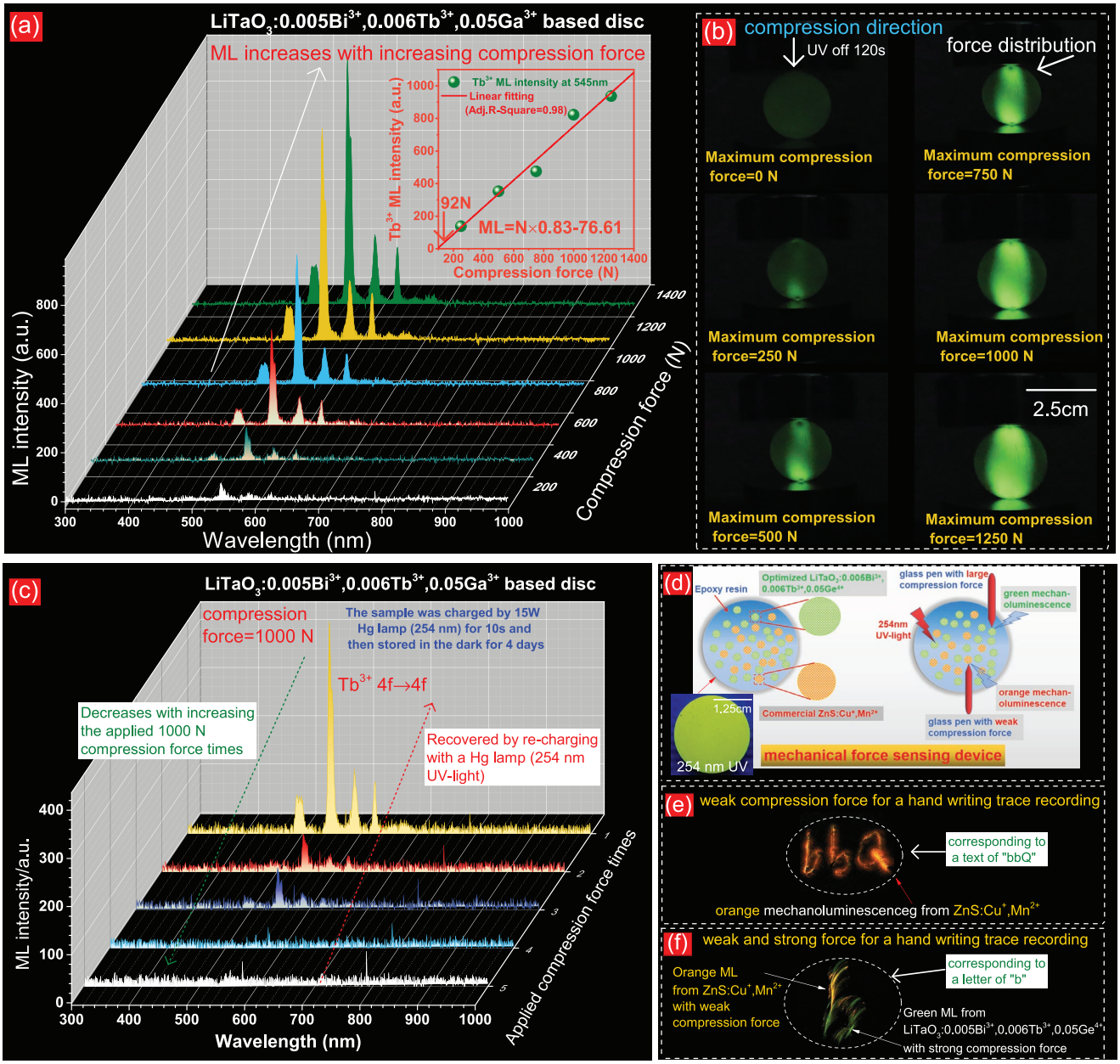

Figure 7. a) Mechanoluminescence (ML) spectra as a function of compression force, b) demonstration of compression force distribution monitoring, and c) repeatability test of ML spectra for the optimized $LiTaO_3$:0.005Bi^{3+},0.006Tb^{3+},0.05Ga^{3+} dispersed in a hard epoxy resin disc after 254 nm UV-light charging. d–f) Proof-of-concept color-tailorable recording of a hand writing trace for anti-counterfeiting application by using different color MLs from the $LiTaO_3$:0.005Bi^{3+},0.006Tb^{3+},0.05Ge^{4+} and commercial ZnS:Cu^{+},Mn^{2+} dispersed in a hard epoxy resin disc.

and ≈1.52 eV deep hole capturing centers. The RT isothermal afterglow spectra of $LiTaO_3$:0.005Bi^{3+},xTb^{3+} (x = 0.0005–0.012) and $LiTaO_3$:0.01Tb^{3+} in Figure S4b,c (Supporting Information) show that the recombination luminescence comes from the characteristic Tb^{3+} 4f→4f emissions. Figure 1a shows that during X-ray or 254 nm UV-light charging, Bi^{3+} can act as an ≈0.62 eV deep electron capturing center, denoted as trap I, to form Bi^{2+} as illustrated by arrow 2a. The electron release process from Bi^{2+}, as illustrated by arrow 3a, was studied in Bi^{3+} and/or Ln^{3+} (Ln = Tb or Pr) doped $LiTaO_3$ in Figure 4 in ref. [17] where a TL glow peaked at ≈283 K and extending from 225 to ≈320 K appears. This means that electron liberation from Bi^{2+} and recombination with the hole captured at the Tb^{4+} ion will partly contribute to the TL glow peak near 315 K in Figure 1b,c. Figure 1c and Figure S13b (Supporting Information) show that common TL glow peaks at ≈322, ≈400, and ≈467 K appear in all the $LiTaO_3$:0.005Bi^{3+},xTb^{3+} (x = 0.0005–0.012) and the $LiTaO_3$:yTb^{3+} (y = 0.001–0.015) samples after X-ray charging. Similar TL glow peaks appear in the $LiTaO_3$:0.005Bi^{3+}, 0.006Tb^{3+},0.05Ga^{3+} and $LiTaO_3$:0.005Bi^{3+},0.006Tb^{3+},0.05Ge^{4+} in Figure 2a,c. We therefore assign the TL glow peaks at ≈322 (0.65 eV), ≈400 (0.81 eV), and ≈467 K (0.96 eV) to unintended

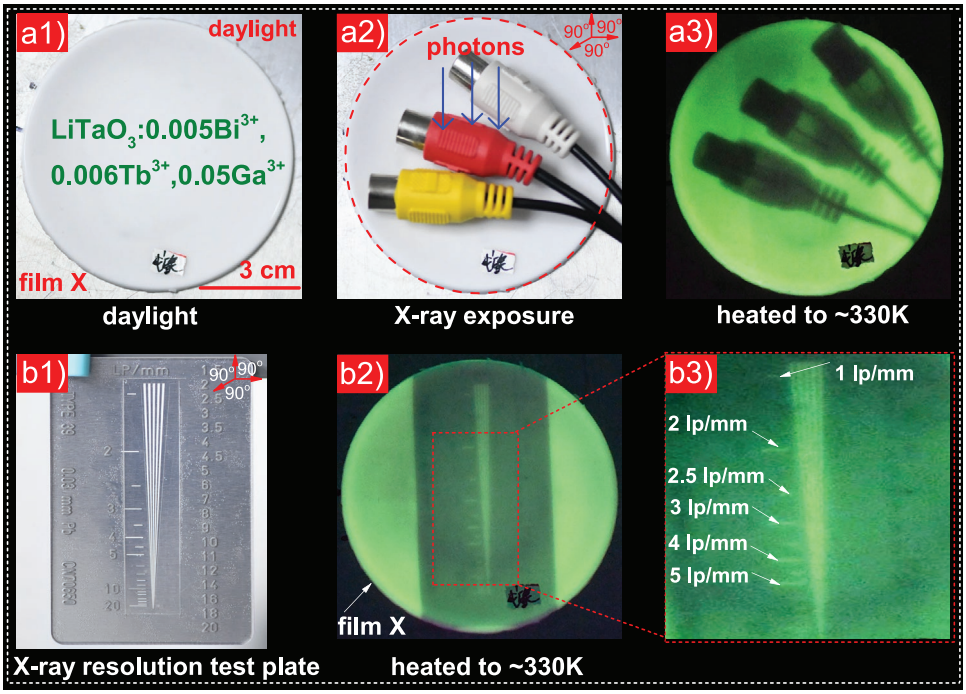

Figure 8. Proof-of-concept information storage by using the optimized $LiTaO_3$:0.005Bi^{3+},0.006 Tb^{3+},0.05Ga^{3+} based flexible silicone gel film after X-ray charging. An X-ray photograph of a3) an electronic plug. b1–b3) Resolution test of the used silicone gel film for X-ray imaging.

defects that act as the electron capturing centers. Their level locations are illustrated in the VRBE diagram of $LiTaO_3$ in Figure 1a. They are collectively denoted as traps II in Figure 1a. The presence of the trap depths II distribution was further evidenced by a TL glow peak cleaning method as demonstrated in Figure S31 (Supporting Information). The free electrons at the conduction band bottom can be captured by traps II as illustrated by arrow 2b during X-ray or 254 nm UV-light charging. Since the energy of the stimulation sources from 850 nm (≈1.46 eV) infrared laser to 365 nm (≈3.40 eV) UV-light is larger than the trapping depth of ~0.65 until 0.96 eV, the electrons captured at traps II can be liberated, as illustrated by arrow 3b in Figure 1a, to recombine with the holes captured at Tb^{4+}, yielding characteristic Tb^{3+} 4f→4f emissions. This process is verified in different Bi^{3+} and Tb^{3+} co-doped $LiTaO_3$ compounds as shown in Figure 2e,f and Figures S16–S18 (Supporting Information).

The TL glow curves of $LiTaO_3$:0.01Tb^{3+} first charged by 254 nm UV-light and then followed by grinding with different durations are shown in Figure 5d. It demonstrates that the charge carriers stored in traps II in Figure 1a can also be liberated by mechanical force stimulation. This charge carrier release process is further verified by the ML spectra when 1000 N compression force is applied repeatedly to the $LiTaO_3$:0.01Tb^{3+} based disc in Figure 5e and for $LiTaO_3$:0.005Bi^{3+},0.006Tb^{3+},0.05Ga^{3+} based disc in Figure 7c. The above results suggest that the ML in Bi^{3+}, Tb^{3+}, Ga^{3+}, or Ge^{4+} doped $LiTaO_3$ compounds in Figures 5–7 is related to the release process of stored charge carrier when compression force was applied.

Figure 4a,b shows the TL glow curves for $LiTaO_3$:0.005Bi^{3+}, 0.006Tb^{3+},0.05Ga^{3+}, and $LiTaO_3$:0.005Bi^{3+},0.006Tb^{3+},0.05Ge^{4+} charged by grinding in an agate mortar. It indicates that there is a force-induced charge carrier storage process, which is rarely reported.[16] The same applies to other Tb^{3+} or/and Bi^{3+} doped $LiTaO_3$ compounds as verified in Figures S20–S24 (Supporting Information). The level locations of unintended defects, collectively denoted as traps III with trapping depth ranging from ≈0.73 to 1.30 eV, are illustrated in Figure 1a. Free charge carriers are created during grinding in an agate mortar, possibly by triboelectricity or piezoelectricity-induced excitation processes.[2a,6,16] The free electrons at the conduction band bottom are captured by traps III as illustrated by arrow 2c, while the free holes at the valence band top can be trapped by Tb^{3+} forming Tb^{4+} as illustrated by the arrow 1a. Because the Tb^{3+} hole trapping depth is larger than the electron trapping depth (≈0.73 until ≈1.30 eV) in the unintended defects (traps III), the electrons captured at traps III are liberated, as illustrated by arrow 3c, to recombine with the hole captured at Tb^{4+} to generate the characteristic Tb^{3+} 4f→4f emissions during TL-readout. The commercial ZnS:Cu^{+},Mn^{2+} was charged by grinding in an agate mortar with 0–600 s duration. Different than in ref. [16], no TL signal was observed in ZnS:Cu^{+},Mn^{2+} from 303 to 723 K. Possibly the bandgap of ZnS (≈3.6 eV) is too small and deep traps cannot be formed during compound synthesis.

3.2. Evaluating the Developed Phosphors for X-Ray Imaging, Stress Distribution Sensing, and Anti-Counterfeiting Applications

The ratio of the integrated TL intensity between 303 and 700 K of the $LiTaO_3$:0.01Tb^{3+} in Figure 1c, the $LiTaO_3$:0.005Bi^{3+},0.006Tb^{3+},0.05Ga^{3+} in Figure 2a, or the optimized $LiTaO_3$:0.005Bi^{3+},0.006Tb^{3+},0.05Ge^{4+} in Figure 2c after X-ray charging to that of the commercial BaFBr(I):Eu^{2+} is ≈1.6, 1.2, and 2.7, respectively. It means that the developed phosphors have excellent charge carrier storage capacities during X-ray excitation. The integrated TL intensity linearly increases with increasing X-ray exposure time as demonstrated in Figure 2d

and Figure S14b (Supporting Information), suggesting that the developed phosphors can be used as potential dosimeters for X-ray detection. The developed phosphors have good chemical stability after exposure to water with a duration of 1 h in Figure S29 (Supporting Information). Therefore, the developed phosphors have potential application in X-ray imaging as demonstrated in Figure 8 and Figure S30 (Supporting Information). The stored charge carriers in the developed phosphors can be efficiently liberated by a wide range energy photon stimulation as demonstrated in Figure 2e–g, and S16. An X-ray imaging photograph is to be expected by reading out the stored charge carriers in the phosphor-based film with photon stimulation. RT afterglow is related to the relatively shallow electron traps. TL glow curves of $LiTaO_3$:0.005Bi^{3+},0.006Tb^{3+},0.05Ge^{4+} with optical stimulation in Figure 2e and Figure S16d–g (Supporting Information) show that the TL peak at ≈325 K slightly shifts toward ≈323 K and the TL peak at about 397 K slightly increases with 850 nm stimulation. This indicates that there is a redistribution of charge carriers by 850 nm stimulation. For WLED and 656 nm stimulation, such redistribution of charge carriers was not observed and the stored charge carriers from deep traps are mainly liberated to yield most of the emission from 60 to 180 s as demonstrated in Figure 2f1.

In Figure 5b2,b3, afterglow and ML is not well separable in the $LiTaO_3$:0.005Bi^{3+},0.001Tb^{3+} based disc. This is because it mainly contains shallow traps with a TL glow peak at ≈329 K, which leads to strong initial Tb^{3+} afterglow after 254 nm UV-light charging as demonstrated in Figure 1b and its insets. In Figure 7b, the distinction of afterglow and ML is much better for the $LiTaO_3$:0.005Bi^{3+},0.006Tb^{3+},0.05Ga^{3+} based disc. The TL glow curves of $LiTaO_3$:0.005Bi^{3+},0.006Tb^{3+},0.05Ga^{3+} in Figure 2a,b show that it contains less shallow traps and more deep traps. When compression force is applied, the liberation of stored charge carriers from the deep traps then contributes to the dominating ML.

4. Conclusions

In this work, Bi^{3+}, Tb^{3+}, Ga^{3+}, or Ge^{4+} doped $LiTaO_3$ perovskite storage phosphors with high charge carrier storage capacity were developed. Based on the vacuum referred binding energy (VRBE) diagram of $LiTaO_3$ containing the energy level locations of unintended defects, Tb^{3+}, Bi^{2+}, and Bi^{3+} in Figure 1a, the charge carrier trapping and release processes were explained. In $LiTaO_3$:0.005Bi^{3+},xTb^{3+} and $LiTaO_3$:yTb^{3+},Tb^{3+} acts as the hole capturing and recombination centre, while Bi^{3+} and unintended defects act as the electron trapping centers. Electron liberation from Bi^{2+} and recombination with the hole captured at Tb^{4+} partly contributes to the TL glow band peaked near 320 K in $LiTaO_3$:0.005Bi^{3+},xTb^{3+} at $\beta = 1$ K/s after X-ray or 254 nm UV-light charging. TL glow curves peaked at ≈322, ≈400, and ≈467 K are assigned to unintended defects II in Figure 1a. The amount of the unintended defects II can be increased by Ga^{3+} or Ge^{4+} co-doping and optimizing compound synthesis temperature. The ratio of the integrated TL intensity after X-ray charging of the optimized $LiTaO_3$:0.005Bi^{3+}, 0.006Tb^{3+},0.05Ga^{3+} or $LiTaO_3$:0.005Bi^{3+},0.006Tb^{3+},0.05Ge^{4+} to that of the state-of-the-art BaFBr(I):Eu^{2+} is ≈1.2 and 2.7, respectively. More than 40h Tb^{3+} afterglow is measurable in the optimized $LiTaO_3$:0.005Bi^{3+},0.001Tb^{3+} and $LiTaO_3$:0.005Bi^{3+}, 0.006Tb^{3+},0.05Ge^{4+} after X-ray or 254 nm UV-light charging. A force-induced charge carrier storage phenomenon appears in the Bi^{3+}, Tb^{3+}, Ga^{3+}, or Ge^{4+} doped $LiTaO_3$ by grinding. A linear relation between the amount of stored charge carriers and the grinding time in an agate mortar appears. ML (ML) appears in Bi^{3+}, Tb^{3+}, Ga^{3+}, or Ge^{4+} doped $LiTaO_3$. The optimized $LiTaO_3$:0.005Bi^{3+},0.006Tb^{3+},0.05Ga^{3+} and $LiTaO_3$:0.005Bi^{3+}, 0.006Tb^{3+},0.05Ge^{4+} show both the strongest TL and ML intensity. The ML process is related to the release of the stored charge carrier when compression force was applied. We also demonstrated that the stored charge carriers can be liberated by a wide energy range photon stimulation from 365 nm UV (3.40 eV) to 850 nm infrared laser (1.46 eV). Proof-of-concept compression force distribution sensing and X-ray imaging were demonstrated by using optimized $LiTaO_3$:0.005Bi^{3+}, 0.006Tb^{3+},0.05Ga^{3+} dispersed in a hard epoxy resin disc and in a silicone gel film. Proof-of-concept color-tailorable ML for anti-counterfeiting was demonstrated by using the commercial ZnS:Cu^{+},Mn^{2+} and the optimized $LiTaO_3$:0.005Bi^{3+},0.006Tb^{3+}, 0.05Ge^{4+} based disc. This work not only reports Bi^{3+}, Tb^{3+}, Ga^{3+}, or Ge^{4+} doped $LiTaO_3$ perovskite with excellent charge carrier storage capacity, but also can accelerate the development of new storage and ML phosphors for X-ray imaging, stress sensing, and non-real-time recording.

5. Experimental Section

All used raw chemicals were purchased from Shanghai Aladdin chemical company. The Tb^{3+} and/or Bi^{3+} doped $LiTaO_3$ crystals were synthesized by using a high-temperature solid-state reaction method. To optimize compression force-induced luminescence (ML) intensities, co-doping of gallium, germanium, niobium, or tin in $LiTaO_3$:0.005Bi^{3+},0.006Tb^{3+} was exploited. The appropriate stoichiometric mixture of Ta_2O_5 (99.99%), Bi_2O_3 (99.99%), Tb_4O_7 (99.99%), Li_2CO_3 (99.99%), Ga_2O_3 (99.99%), Nb_2O_5 (99.99%), GeO_2 (99.99%), or SnO (99.99%) was weighed, ground, and mixed well with the help of acetone solution in an agate mortar. The homogeneously mixed mixture was then kept at 1250 °C for a duration of 6 h in a covered corundum crucible under ambient atmosphere. The utilized heating rate for the furnace was 3 °C min^{-1}. After that, the synthesized compounds were naturally cooled to room temperature (RT) and then homogeneously ground for further measurements. Nb^{5+} and Sn^{2+} as co-dopants appeared to deteriorate TL and ML properties, and were not further studied. To optimize the ML intensity in $LiTaO_3$:0.005Bi^{3+},0.006Tb^{3+},0.05Ge^{4+}, it was synthesized at 1275 °C with a duration of 6 h. To investigate compression force-induced luminescence properties, ≈0.8 g afterglow phosphor like $LiTaO_3$:0.005Bi^{3+},xTb^{3+} was dispersed well in ≈6.4 g epoxy resin to produce a hard disc with a diameter of ≈2.5 cm and a thickness of ≈0.6 cm by using a silicon gel-based flexible mold. The mold filled with the phosphor and epoxy resin was kept at 80 °C in vacuum for a duration of 2.5 h. To verify proof-of-concept X-ray imaging application, ≈0.6 g the optimized $LiTaO_3$: 0.005Bi^{3+},0.006Tb^{3+},0.05Ga^{3+} afterglow phosphor was dispersed in ≈4.0 g silicone gel (Sylgard 184, Dow Corning) to make a flexible film with a diameter of ≈6 cm on a polished sapphire substrate. The substrate was heated at ≈70 °C with a duration of 3 h in vacuum. The substrate was removed from the flexible film prior to X-ray imaging. A state-of-the-art ZnS:Cu^{+}, Mn^{2+} phosphor was purchased from Shanghai keyan phosphor technology company. The ZnS:Cu^{+},Mn^{2+}, optimized $LiTaO_3$:0.005Bi^{3+}, 0.006Tb^{3+},0.05Ge^{4+}, and epoxy resin were mixed well in a mold to make a hard epoxy resin disc for anti-counterfeiting application. The afterglow,

ML, and X-ray imaging photographs were taken by an iPhone 13Pro or a Nikon D850 camera in the dark. For X-ray imaging measurements, a TUB00154-9I-W06 tube (MOXTEK, Ltd.) was utilized. It operated at 60 kV, 200 μA, and 12 W. The X-ray imaging films were charged by the X-rays with a duration of 180 s in the dark.

The phase purities of all synthesized compounds were verified with a Japan Rigaku Smar/SmartLa X-ray diffraction setup. It contains an X-ray tube that operates at 40 kV and 30 mA. The scanning electron microscope (SEM) and energy-dispersive X-ray spectroscopy images were recorded with a Japan JEOL JSM-7610FPlus electron microscope. Photoluminescence excitation (PLE) spectra, emission spectra (PL), room temperature (RT) isothermal decay spectra, and curves were recorded by using an FLS920 fluorescence spectrometer (Edinburgh Instruments Ltd.). All measured photoluminescence excitation spectra had been corrected by the wavelength-dependent excitation intensity of the utilized xenon lamp in the FLS920 spectrometer. The compression force-induced luminescence (ML) spectra were recorded in the dark with a facility, which combined a UV/near-infrared spectrometer (Ocean Optics, type QE65Pro) in the spectral range between 200 and 1000 nm and a computer program-controlled testing machine (10 kN, CMT1104, Zhuhai SUST Electrical Equipment Co., Ltd).[10] This facility was shown in Figure S32 (Supporting Information). Prior to the ML measurements, all prepared phosphors dispersed in hard epoxy resin discs were charged by a 15 W Hg lamp (254 nm UV-light) with a duration of 60 s and then faded in the dark with a duration of 120 s in order to decrease the effect of the afterglow on the ML results. The obtained ML spectra have been corrected by the weak afterglow background. The epoxy resin disc was compressed at a rate of 10 cm min^{-1} to quickly generate the maximum force of 1000 N during ≈3 s. An integrated time for the QE65Pro spectrometer was fixed at 0.80 s during ML measurements. The ML intensity decayed within few seconds when compression force was applied.

X-ray excited integrated emission intensities in the spectral range from 200 to 700 nm as a function of time, above 300 K thermoluminescence (TL) glow curves, and room temperature isothermal decay curves were measured. The employed setup combined a thermostat in the temperature range from 300 to 773 K, a Hg lamp (254 nm UV-light), a voltage adjustable TUB00083-2 X-ray tube (MOXTEK, Ltd.) operated at 30 kV, 50 μA, and 1.5 W, a BG-39 filter (SCHOTT Ltd.), and a R928P photomultiplier (Japan Hamamatsu Ltd.) that could detect a photon energy range from 200 to 860 nm. About 0.0300 g phosphor was used for the above measurements. To study the charge carrier storage property when compression force was applied, a phosphor was charged by grinding in an agate mortar with different duration time in the dark prior to TL measurements. For the measurements of optically stimulated RT isothermal decay curves and TL glow curves, different energy light sources of a commercial white-LED (WLED), a ≈396 nm LED, a ≈365 nm UV lamp, 850 nm laser, and red 656 nm laser had been utilized. Prior to all TL measurements, all compounds were heated to ≈723 K and kept at that temperature for 200 s in order to remove captured electrons and holes from traps and then cooled to ≈298 K. The measured TL intensities had been corrected by the used compound mass and the charging time of the X-ray or 254 nm UV-light.

To verify electron and hole capturing processes, a thermoluminescence excitation (TLE) curve was recorded by utilizing the FLS920 fluorescence spectrometer.[29] Different energy photons in the spectral range from 200 to 400 nm were utilized to charge the $LiTaO_3$:0.005Bi^{3+},0.001Tb^{3+} afterglow phosphor with a duration of 60 s, and then room temperature isothermal decay curves (λ_{em} = 544 nm) were measured during 62 s in the dark. The integrated Tb^{3+} 544 nm RT isothermal decay intensities between 0 and 62 s had been corrected for the excitation intensity of the utilized Hamamatsu CW xenon lamp in the FLS920 spectrometer.

Supporting Information

Supporting Information is available from the Wiley Online Library or from the author.

Acknowledgements

T.L. acknowledges the financial supports from the National Natural Science Foundation of China (No. 12104170), the Fundamental Research Funds for the Central Universities (No. ZQN-1023), and the Scientific Research Funds of Huaqiao University (No. 21BS106). This work was partly supported by the Instrumental Analysis of Huaqiao University. T.L. thanks Prof. Huanghao Yang and Prof. Qiushui Chen from Fuzhou University for their help with X-ray imaging measurements.

Conflict of Interest

The authors declare no conflict of interest.

Data Availability Statement

The data that support the findings of this study are available on request from the corresponding author. The data are not publicly available due to privacy or ethical restrictions.

Keywords

Bi^{3+}, color-tailorable mechanoluminescence, force induced charge carrier storage, $LiTaO_3$ perovskites, Tb^{3+}, X-ray imaging

Received: May 26, 2022
Revised: June 23, 2022
Published online:

[1] a) Y. Zhuang, R.-J. Xie, *Adv. Mater.* **2021**, *33*, 2005925; b) B. P. Chandra, K. K. Shrivastava, *J. Phys. Chem. Solids* **1978**, *39*, 939; c) P. Jha, B. P. Chandra, *Luminescence* **2014**, *29*, 977; d) A. S. Herschel, *Nature* **1899**, *60*, 29; e) W. Wang, Z. Wang, J. Zhang, J. Zhou, W. Dong, Y. Wang, *Nano Energy* **2022**, 106920.
[2] a) J.-C. Zhang, X. Wang, G. Marriott, C.-N. Xu, *Prog. Mater. Sci.* **2019**, *103*, 678; b) G. T. Reynolds, *J. Lumin.* **1997**, *75*, 295.
[3] a) J. Li, C.-N. Xu, D. Tu, X. Chai, X. Wang, L. Liu, E. Kawasaki, *Acta Mater.* **2018**, *145*, 462; b) C. T. Butler, *Phys. Rev.* **1966**, *141*, 750; c) S. Zhou, Y. Cheng, J. Xu, H. Lin, W. Liang, Y. Wang, *Laser Photonics Rev* **2022**, *16*, 2100666.
[4] C. N. Xu, T. Watanabe, M. Akiyama, X. G. Zheng, *Appl. Phys. Lett.* **1999**, *74*, 1236.
[5] C.-N. Xu, T. Watanabe, M. Akiyama, X.-G. Zheng, *Appl. Phys. Lett.* **1999**, *74*, 2414.
[6] D. Tu, C.-N. Xu, A. Yoshida, M. Fujihala, J. Hirotsu, X.-G. Zheng, *Adv. Mater.* **2017**, *29*, 1606914.
[7] X. Yang, R. Liu, X. Xu, Z. Liu, M. Sun, W. Yan, D. Peng, C.-N. Xu, B. Huang, D. Tu, *Small* **2021**, *17*, 2103441.
[8] a) C. Chen, Y. Zhuang, D. Tu, X. Wang, C. Pan, R.-J. Xie, *Nano Energy* **2020**, *68*, 104329; b) Y. Zheng, X. Li, R. Ma, Z. Huang, C. Wang, M. Zhu, Y. Du, X. Chen, C. Pan, B. Wang, Y. Wang, D. Peng, *Small* **2022**, 2107437; c) D. Peng, Y. Jiang, B. Huang, Y. Du, J. Zhao, X. Zhang, R. Ma, S. Golovynskyi, B. Chen, F. Wang, *Adv. Mater.* **2020**, *32*, 1907747; d) Y. Du, Y. Jiang, T. Sun, J. Zhao, B. Huang, D. Peng, F. Wang, *Adv. Mater.* **2019**, *31*, 1807062; e) Y.-L. Yang, T. Li, F. Guo, J.-Y. Yuan, C.-H. Zhang, Y. Zhou, Q.-L. Li, D. Y. Wan, J.-T. Zhao, Z.-J. Zhang, *Inorg. Chem.* **2022**, *61*, 4302; f) Y.-L. Yang, Q.-L. Li, X.-C. Yang, W. Yang, R. An, T. Li, Y. Zhou, H.-W. Zhang, J.-T. Zhao, Z.-J. Zhang, *J. Mater. Chem. C* **2020**.

[9] S. Liu, R. Liu, X. Yang, J. Li, M. Sun, C.-N. Xu, B. Huang, Y. Liang, D. Tu, *Nano Energy* **2021**, 106799.
[10] P. Xiong, B. Huang, D. Peng, B. Viana, M. Peng, Z. Ma, *Adv. Funct. Mater.* **2021**, *31*, 2010685.
[11] H. Chen, L. Wu, T. Sun, R. Dong, Z. Zheng, Y. Kong, Y. Zhang, J. Xu, *Appl. Phys. Lett.* **2020**, *116*, 051904.
[12] J.-C. Zhang, X.-Y. Xue, Y.-F. Zhu, S. Wang, H.-W. He, X. Yan, X. Ning, D. Wang, J. Qiu, *Chem. Eng. J. 406*, 126798.
[13] J. Ning, Y. Zheng, Y. Ren, L. Li, X. Shi, D. Peng, Y. Yang, *Sci. Bull.* **2022**, *67*, 707.
[14] F. Lin, X. Li, C. Chen, X. Pan, D. Peng, H. Luo, L. Jin, Y. Zhuang, R.-J. Xie, *Chem. Mater.* **2022**, *34*, 5311.
[15] C. Wang, R. Ma, D. Peng, X. Liu, J. Li, B. Jin, A. Shan, Y. Fu, L. Dong, W. Gao, Z. L. Wang, C. Pan, *InfoMat* **2021**, *3*, 1272.
[16] Y. Zhuang, D. Tu, C. Chen, L. Wang, H. Zhang, H. Xue, C. Yuan, G. Chen, C. Pan, L. Dai, R.-J. Xie, *Light: Sci. Appl.* **2020**, *9*, 182.
[17] T. Lyu, P. Dorenbos, *Laser Photonics Rev.* **2022**, 2200304.
[18] a) T. Lyu, P. Dorenbos, *Chem. Eng. J.* **2019**, *372*, 978; b) T. Lyu, P. Dorenbos, *Chem. Eng. J.* **2020**, 124776; c) T. Lyu, P. Dorenbos, *J. Mater. Chem. C* **2018**, *6*, 6240; d) A. Dobrowolska, A. J. J. Bos, P. Dorenbos, *Phys. Status Solidi RRL* **2019**, *13*, 1800502; e) D. Van der Heggen, R. Zilenaite, E. Ezerskyte, V. Fritz, K. Korthout, D. Vandenberghe, J. De Grave, J. Garrevoet, L. Vincze, D. Poelman, J. J. Joos, P. F. Smet, *Adv. Funct. Mater* **2022**, *32*, 2109635.
[19] a) C. Richard, B. Viana, *Light: Sci. Appl.* **2022**, *11*, 123; b) S. Liu, N. Mao, Z. Song, Q. Liu, *ACS Appl. Mater. Interfaces* **2022**, *14*, 1496; c) Z. Yang, J. Hu, D. Van der Heggen, A. Feng, H. Hu, H. Vrielinck, P. F. Smet, D. Poelman, *Adv. Funct. Mater* **2022**, 2201684.
[20] a) T. Lyu, P. Dorenbos, C. Li, S. Li, J. Xu, Z. Wei, *Chem. Eng. J.* **2022**, *435*, 135038; b) S. Lin, H. Lin, Q. Huang, Y. Cheng, J. Xu, J. Wang, X. Xiang, C. Wang, L. Zhang, Y. Wang, *Laser Photonics Rev.* **2019**, *13*, 1900006.
[21] P. Dorenbos, *ECS J. Solid State Sci. Technol.* **2021**, *10*, 086002.
[22] P. Dorenbos, *Phys. Rev. B* **2012**, *85*, 165107.
[23] a) P. Dorenbos, *ECS J. Solid State Sci. Technol.* **2013**, *2*, R3001; b) P. Dorenbos, *J. Lumin.* **2020**, *222*, 117164; c) J. Ueda, P. Dorenbos, A. J. J. Bos, K. Kuroishi, S. Tanabe, *J. Mater. Chem. C* **2015**, *3*, 5642.
[24] M. Grinberg, J. Barzowska, Y. Shen, K. L. Bray, *Phys. Rev. B* **2001**, *63*, 214104.
[25] a) M. Nikl, R. Morlotti, C. Magro, R. Bracco, *J. Appl. Phys.* **1996**, *79*, 2853; b) G. Qiu, H. Ye, X. Wang, H. Fang, Y. Li, X. Yao, *Ceram. Int.* **2019**, *45*, 8553; c) S. Tian, P. Feng, S. Ding, Y. Wang, Y. Wang, *J. Alloys Compd.* **2022**, *899*, 163325.
[26] a) R. Hu, Y. Zhang, Y. Zhao, X. Wang, G. Li, C. Wang, *Chem. Eng. J.* **2020**, *392*, 124807; b) R. Hu, Y. Zhao, Y. Zhang, X. Wang, G. Li, M. Deng, *Appl. Mater. Today.* **2022**, *26*, 101376.
[27] T. Lyu, P. Dorenbos, *Chem. Mater.* **2020**, *32*, 1192.
[28] P. Dorenbos, *J. Lumin.* **2018**, *197*, 62.
[29] a) D. Kulesza, A. J. J. Bos, E. Zych, *Acta Mater.* **2022**, 117852; b) A. J. J. Bos, R. M. van Duijvenvoorde, E. van der Kolk, W. Drozdowski, P. Dorenbos, *J. Lumin.* **2011**, *131*, 1465.
[30] X. Ou, X. Qin, B. Huang, J. Zan, Q. Wu, Z. Hong, L. Xie, H. Bian, Z. Yi, X. Chen, Y. Wu, X. Song, J. Li, Q. Chen, H. Yang, X. Liu, *Nature* **2021**, *590*, 410.
[31] A. Qasem, P. Xiong, Z. Ma, M. Peng, Z. Yang, *Laser Photonics Rev.* **2021**, *15*, 2100276.